Dalton Transactions

PAPER

View Article Online
View Journal

Cite this: DOI: 10.1039/d6dt00558f

Mechanochemical synthesis, solvent-controlled coordination, and catalytic oxidation activity of furoic acid-based Mo(VI) complexes

Josipa Sarjanović, [a] Béla Fiser [b,c,d] and Jana Pisk *[a]

Polynuclear and mononuclear molybdenum(VI) complexes coordinated with water or methanol were synthesized using Schiff base ligands derived from the condensation of 2-furoic hydrazide with 2-hydroxybenzaldehyde (H_2L^1) or 2-hydroxy-5-nitrobenzaldehyde (H_2L^2), emphasising a mechanochemical synthetic pathway. The complexes were characterized using comprehensive spectroscopic techniques, while single-crystal X-ray diffraction provided definitive structural elucidation for $[MoO_2(L^1)(MeOH)]$ (**1**) and $[MoO_2(L^1)(H_2O)]$ (**3**). Thermogravimetric analysis revealed insights into the thermal stability and decomposition pathways of the complexes. DFT calculations showed that solvent donor ability controls Mo(VI) coordination and aggregation, rendering μ-oxo dimer formation thermodynamically unfavourable. The catalytic performance of six Mo(VI) complexes was investigated for the oxidation of benzyl alcohol using *tert*-butyl hydroperoxide (TBHP) in aqueous medium, with systematic optimization of the oxidant-to-substrate ratio. To explore greener alternatives, H_2O_2 was also evaluated as an oxidant, and the influence of acetonitrile as a co-solvent and reaction temperature on catalytic efficiency was thoroughly studied. These results highlight the importance of ligand structure and solvent coordination in modulating catalytic activity. Overall, this study demonstrates that these Mo(VI) complexes serve as highly efficient and tunable catalysts for selective alcohol oxidation under mild and environmentally benign conditions. This work provides new insights into the design of molybdenum-based oxidation catalysts and emphasizes the potential of fine-tuning reaction parameters to achieve optimal catalytic performance.

Received 6th March 2026,
Accepted 15th May 2026

DOI: 10.1039/d6dt00558f

rsc.li/dalton

Introduction

The selective oxidation of primary alcohols to aldehydes is a cornerstone transformation in both laboratory-scale synthesis and industrial chemical production,[1–3] owing to the pivotal role aldehydes play as intermediates and high-value products in the pharmaceutical,[4,5] food,[6] and fragrance industries.[7] Among aromatic aldehydes, benzaldehyde ranks as one of the most significant, second only to vanillin in importance for perfumery and food applications.[8,9] The global benzaldehyde market was valued at about 374.4 million USD in 2024 and is projected to grow at a compound annual growth rate (CAGR) of ~5.6% between 2025 and 2030. In Europe, the demand is expected to increase significantly over the forecast period, driven by rising consumption in the personal care, cosmetics, flavour, fragrance and pharmaceuticals sectors.[10] Consequently, efficient catalytic methods for the synthesis of high-purity benzaldehyde are of considerable interest, particularly those that meet the stringent purity standards required in cosmetics and flavouring industries. Conventionally, benzaldehyde is produced *via* the hydrolysis of benzyl chloride[11] or by the oxidation of toluene.[12] However, these processes suffer from notable drawbacks, including contamination with organic chlorine or benzoic acid, posing environmental and purity concerns. As a result, alternative synthetic approaches that provide chlorine-free, selectively oxidized benzaldehyde have been actively pursued.

In recent decades, both gas-phase and liquid-phase catalytic oxidation of benzyl alcohol (BnOH) to benzaldehyde (BnCHO) has been extensively investigated. Gas-phase oxidation, while effective, is hampered by significant carbon loss due to over-oxidation and the formation of carbon oxides, reducing both selectivity and yield.[13–15] In contrast, liquid-phase oxidation offers superior selectivity and minimizes the formation of undesirable by-products, such as benzoic acid, benzyl benzoate and benzyl ether, making it a more suitable method for producing high-purity benzaldehyde under milder and environmentally benign conditions.[16–18]

[a]*Department of Chemistry, Faculty of Science, University of Zagreb, Horvatovac 102a, 10000 Zagreb, Croatia. E-mail: jana.pisk@chem.pmf.hr*
[b]*Institute of Chemistry, University of Miskolc, 3515 Miskolc-Egyetemváros, Hungary*
[c]*Ferenc Rakoczi II Transcarpathian Hungarian College of Higher Education, 90200 Beregszász, Transcarpathia, Ukraine*
[d]*Department of Physical Chemistry, Faculty of Chemistry, University of Lodz, 90-236 Lodz, Poland*

Liquid-phase catalytic systems often employ molecular oxygen (O_2), hydrogen peroxide (H_2O_2), or *tert*-butyl hydroperoxide (TBHP) in aqueous medium as oxidants, either in the presence or absence of a co-solvent.[19,20–22] The nature of the catalyst and reaction conditions critically influence the selectivity and efficiency of the transformation. Depending on these factors, side reactions such as over-oxidation to benzoic acid and benzoate,[23,24] disproportionation to yield toluene and water,[23,25] and dehydration leading to dibenzyl ether may occur.[26] Therefore, fine-tuning catalytic systems to suppress these side reactions is essential for achieving high selectivity towards benzaldehyde.

Transition metal-based catalysts, including V, Co, Mo, Ni, and Cu, have shown promising activity in this context.[20–22,27,28]

Their use supports the development of more sustainable oxidation processes aligned with green chemistry principles, a key objective of which is to minimize hazardous substances, reduce waste, and improve energy and resource efficiency. Green chemistry also emphasizes the use of safer reagents and methodologies that lower the environmental impact while maintaining high reaction efficiency and selectivity. Applying these principles ensures that reactions are not only effective, but also environmentally responsible, meeting both industrial performance requirements and regulatory standards for safety and purity. One approach that embodies the principles of green chemistry is mechanochemical synthesis, which aligns closely with these goals by enabling solvent-free or low-solvent use for the preparation of catalysts for oxidation reactions.

Our recent investigation has shown that vanadium coordination complexes exhibit high conversion efficiency in the oxidation of benzyl alcohol; however, they often suffer from poor selectivity over extended reaction times due to overoxidation to benzoic acid.[20,21] To address this limitation, we aimed to synthesize novel molybdenum coordination complexes as selective catalysts for the oxidation of benzyl alcohol, with the goal of minimizing overoxidation. For this purpose, 2-furoic hydrazide was employed as a ligand constituent (Scheme 1). Notably, coordination complexes of this type of hydrazide are mostly coordinated to V,[29–31] Pd,[32,33] Sn,[34,35] or Cu centres,[36,37] with only a few structures reported for Mo,[38,39] highlighting the novelty of our investigation. The aim of this work is twofold: (i) to prepare simple molybdenum-based coordination complexes with a 2-furoic hydrazide ligand (SI Scheme X) that is sporadically represented in the literature and (ii) to investigate their catalytic performance in the selective oxidation of benzyl alcohol to benzaldehyde.

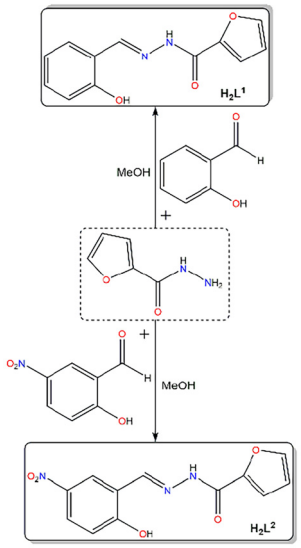

Scheme 1 Solution-based synthesis of the ligands used for the presented investigation.

Results and discussion

Synthesis, infrared spectroscopy and thermal characterisation of ligands and molybdenum(VI) compounds

The ligands $\mathbf{H_2L^1}$ and $\mathbf{H_2L^2}$ were synthesized mechanochemically by the reaction of 2-furoic hydrazide with salicylaldehyde and 2-hydroxy-5-nitrobenzaldehyde, respectively (Scheme 1). The reactions were carried out in the presence of a small amount of solvent (20 μL of MeOH for $\mathbf{H_2L^1}$ and 30 μL of MeOH or EtOH for $\mathbf{H_2L^2}$) at 25 Hz for 30 min. In parallel, a conventional solution-based synthesis in methanol was also employed in an attempt to obtain single crystals. The solution-based synthesis provided good yields of 61% for $\mathbf{H_2L^1}$ and 77% for $\mathbf{H_2L^2}$. Notably, a suitable single crystal of the brown ligand $\mathbf{H_2L^1}$ was successfully obtained, enabling the determination of its crystal and molecular structure (*vide infra*).

DSC analysis provided insight into the ligands' melting point and purity (SI Fig. S1 and S2). The DSC curve of the ligand $\mathbf{H_2L^1}$ exhibited a sharp endothermic peak at 173 °C, while that of the ligand $\mathbf{H_2L^2}$ showed a sharp endothermic peak at 277 °C. In both cases, the endothermic peak was attributed to the melting process. The absence of secondary peaks in both thermograms confirmed the completion of the reactions and the high purity of the obtained ligands. Infrared attenuated total reflectance (IR-ATR) spectroscopy further confirmed the successful formation of the ligands (SI Fig. S3 and S4). A strong absorption band corresponding to the C═O stretching vibration was observed at 1655 cm^{-1} for the ligand $\mathbf{H_2L^1}$ and at 1669 cm^{-1} for the ligand $\mathbf{H_2L^2}$, indicating the presence of the keto form. The C═N (imine) stretching bands were recorded at 1609 cm^{-1} ($\mathbf{H_2L^1}$) and 1611 cm^{-1} ($\mathbf{H_2L^2}$). Broad bands centred at 3228 cm^{-1} ($\mathbf{H_2L^1}$) and 3275 cm^{-1} ($\mathbf{H_2L^2}$) were attributed to O–H stretching vibrations from the phenolic group.[40,41] Comparison of the ligands obtained by solution-based synthesis and mechanochemical synthesis was confirmed by IR-ATR spectroscopy (SI Fig. S5 and S6).

Following the successful mechanochemical synthesis of both ligands ($\mathbf{H_2L^{1\ or\ 2}}$), the same green chemistry approach was applied to the mechanochemical preparation of molybdenum complexes. Two molybdenum complexes were successfully obtained using this method.

The orange complex was synthesized by milling the ligand $\mathbf{H_2L^1}$ with $[MoO_2(acac)_2]$ for 60 min at 25 Hz with 30 μL of MeOH. IR analysis of the obtained compound indicated that all the precursors reacted completely. Subsequently, reactions involving the same molybdenum starting compound and the ligand $\mathbf{H_2L^2}$ were investigated. After optimization of the reaction conditions (see SI Table S1), the yellow complex was also successfully synthesized mechanochemically. This reaction required 120 min of milling at 25 Hz with the addition of 30 μL of MeOH, with a 10 min pause after 60 min during which the milling jar was opened. Opening the jar allowed the release of volatile byproducts, such as acetylacetone, thereby preventing pressure buildup and excessive heating during the milling process. Consequently, solution-based synthesis was explored, in which ligands $\mathbf{H_2L^1}$ or $\mathbf{H_2L^2}$ reacted with $[MoO_2(acac)_2]$ in a 1 : 1 molar ratio in various solvents (see SI Scheme S1). Reactions of $\mathbf{H_2L^1}$ with the $\{MoO_2\}^{2+}$ core yielded an orange complex, while $\mathbf{H_2L^2}$ resulted in the formation of a yellow complex, regardless of the solvent used (methanol, acetonitrile, dichloromethane or acetone). IR-ATR spectra of complexes synthesized in non-methanolic solvents were identical, indicating that the same products were obtained regardless of solvent choice.

Characterization of the orange complex (**1**), obtained from MeOH with $\mathbf{H_2L^1}$, and the yellow complex (**2**), obtained from MeOH with $\mathbf{H_2L^2}$, revealed C=N stretching bands at 1609 and 1614 cm^{-1}, respectively (SI Fig. S7 and S8). C–O stretching appeared at 1271 cm^{-1} for orange complex (**1**) and 1272 cm^{-1} for yellow complex (**2**), suggesting coordination through ONO donor atoms.[35,42,43–45] The sharp Mo=O asymmetric stretching vibrations were observed at 910 and 898 cm^{-1} for the orange complex (**1**), and at 939 and 913 cm^{-1} for the yellow complex (**2**). A distinct band at 1046 cm^{-1} (**1**) and 1054 cm^{-1} (**2**) implies the presence of a coordinated methanol molecule.[46,47]

Thermogravimetric analysis (TGA) results for complexes (**1**) and (**2**) are presented in SI Table S2. The calculations were performed using the proposed molecular formula $[MoO_2(L^{1\text{ or }2})(MeOH)]$ based on the IR-ATR data. The orange complex (**1**) exhibited a two-step weight loss, as shown in SI Fig. SX. The first step, observed between 140 °C and 235 °C, corresponded to the release of MeOH, with a mass loss of 8.57% (calcd 8.24%) and was accompanied by an endothermic peak in the DSC curve. In the second step (280–550 °C), the exothermic peaks observed in the DSC curve were attributed to the decomposition of the complex, as indicated by the TG analysis, leaving a residue of 36.62%, which aligns with the theoretical MoO_3 value of 36.84%. IR-ATR spectra of the residue matched those of commercial MoO_3, confirming its identity. Similarly, the yellow complex (**2**) underwent two decomposition steps (SI Fig. S9 and S10). The first, from 175–210 °C, corresponded to methanol release, with a mass loss of 8.63% (theoretical: 7.39%). This process was additionally observed as an endothermic peak in the DSC curve. The second decomposition stage (305–490 °C) led to a final residue of 33.01%, which aligns with the expected MoO_3 content (29.02%), supporting the formation of $[MoO_2(L^2)(MeOH)]$ (**2**).

For the complexes formed in non-methanolic solvents, similar spectroscopic features were observed (SI Fig. S11 and S12). The orange complex (**3**), from $\mathbf{H_2L^1}$, and the yellow complex (**4**), from $\mathbf{H_2L^2}$, exhibited C=N stretching bands at 1612 cm^{-1} and 1609 cm^{-1}, respectively. C–O stretches were detected at 1270 cm^{-1} (**3**) and 1275 cm^{-1} (**4**), suggesting ONO coordination.[43,44,47] Sharp Mo=O asymmetric bands were found at 909 and 871 cm^{-1} for the orange complex (**3**), and 945 and 918 cm^{-1} for the yellow complex (**4**). Notably, both complexes exhibited additional bands at 1647 cm^{-1} (**3**) and 1633 cm^{-1} (**4**), corresponding to O–H vibrations, indicative of water coordination to the metal center.[47,48] Based on the IR-ATR data, the complex was proposed to have the formula $[MoO_2(L^{1\text{ or }2})(H_2O)]$. The TGA curve of the orange complex (**3**) revealed a first mass loss of 5.11% between 145 and 195 °C, consistent with the loss of one water molecule (calcd 4.81%), see SI Fig. S13. The second stage of decomposition (295–545 °C) resulted in a residue of 38.22%, closely matching the theoretical MoO_3 content of 37.60%. The expected composition for the orange complex is $[MoO_2(L^1)(H_2O)]$ (**3**). The yellow complex (**4**) exhibited similar decomposition behaviour (SI Fig. S14). The first step, occurring between 180 and 215 °C, corresponded to the release of one water molecule, with an observed mass loss of 5.10% (theoretical: 4.29%). The subsequent decomposition between 305 and 465 °C yielded a final residue of 34.12%, in agreement with the theoretical value of 30.16%, confirming the formulation of the yellow complex as $[MoO_2(L^2)(H_2O)]$ (**4**). As in the methanol-coordinated complexes, the first step in the DSC curve showed an endothermic peak attributed to solvent release, followed by exothermic peaks in the second step.

After identification by IR-ATR spectroscopy and TG analysis, which confirmed the molecular formulas of the synthesized complexes, the orange and yellow complexes obtained *via* mechanochemical synthesis were compared with complexes prepared by conventional solution-based methods using IR-ATR spectroscopy (see SI Fig. S15 and S16). The spectroscopic data showed excellent agreement between the mechanochemically and solution-synthesized complexes, and the orange complex was identified as $[MoO_2(L^1)(MeOH)]$ (**1**), while the yellow complex corresponded to $[MoO_2(L^2)(H_2O)]$ (**4**).

Heating any of the methanol- or water-coordinated mononuclear complexes to 250 °C for one hour resulted in the formation of brown complexes (**5**) and (**6**) from $\mathbf{H_2L^1}$ and $\mathbf{H_2L^2}$, respectively. These new complexes remained unchanged upon cooling to room temperature and showed no signs of reverting to the original mononuclear structures. IR-ATR spectra of the brown complex (**5**) showed C=N stretching at 1618 cm^{-1} and C–O at 1270 cm^{-1}, while the brown complex (**6**) showed C=N stretching at 1606 cm^{-1} and C–O at 1263 cm^{-1} (SI Fig. S17 and S18). Broad bands at 856 cm^{-1} (**5**) and 833 cm^{-1} (**6**) were assigned to Mo=O···Mo bridging vibrations, indicative of a polynuclear structure.[43,44,48] The absence of bands related to methanol or water coordination further supports this assignment. Analysis of the IR-ATR data indicated that the complex can be formulated as $[MoO_2(L^{1\text{ or }2})]_n$. When heated under an

oxygen atmosphere, the brown complex (**5**) exhibited a single-step mass loss between 295 and 555 °C, accompanied by an exothermic peak in the DSC curve, resulting in a residue of 41.80%, closely matching the calculated MoO_3 content of 40.26%. Similarly, complex (**6**) decomposed between 315 and 480 °C with an exothermic DSC signal, leaving a residue of 32.05%, in agreement with the calculated value of 35.65%. These results indicate the formation of polynuclear complexes $[MoO_2(L^1)]_n$ (**5**) and $[MoO_2(L^2)]_n$ (**6**) (SI Fig. S19 and S20).

Description of molecular and crystal structures

In this study, three crystal structures were determined (SI Tables S3–S5): the ligand $\mathbf{H_2L^1}$ and two mononuclear dioxomolybdenum(VI) complexes, $[MoO_2(L^1)(MeOH)]$ (**1**) and $[MoO_2(L^1)(H_2O)]$ (**3**). The structure of hydrazone ligand $\mathbf{H_2L^1}$ was previously reported in the database as references CCDC 788397 [49] and 1529788.[50]

The dioxomolybdenum(VI) complexes (SI Fig. S21 and S22), derived from $\mathbf{H_2L^1}$, exhibit structural features consistent with similar literature-known compounds.[44,45,47] In both complexes, the dianionic ligand L^{2-} adopts the enol–imino tautomeric form (SI Table S4) and coordinates *via* an ONO donor set, creating a chelating pocket. The sixth coordination site of the $\{MoO_2\}^{2+}$ core is occupied by a methanol or water molecule. The coordination geometry around molybdenum in both structures is best described as distorted octahedral, defined by *cis*-arranged oxygen atoms, the tridentate ONO ligand, and an ancillary solvent molecule (either water or methanol).

In $[MoO_2(L^1)(MeOH)]$ (**1**) (Fig. 1(a)), the absence of a ditopic hydrogen-bond donor leads to the formation of discrete, non-interacting homodimers. These dimers are stabilized through $O_{MeOH}\cdots H\text{–}N_{amide}$ hydrogen bonds between symmetry-equivalent molecules. Two geometrically distinct but structurally similar dimer types are observed, both further stabilized by weak C–H···O interactions (SI Table S5). Together, they arrange into a zig-zag pattern throughout the crystal lattice, as shown in Fig. S21(b).

In contrast, $[MoO_2(L^1)(H_2O)]$ (**3**) assembles into supramolecular chains through directional hydrogen bonding: $O_w\text{–}H\cdots N_{amide}$ with one neighbouring molecule and $O_w\text{–}H\cdots O{=}Mo$ with another (Fig. 1(b)). These chains are further interconnected by multiple $Mo{=}O_{ax}\cdots H\text{–}C$ contacts, yielding an overall linear arrangement in the solid state (SI Table S4).

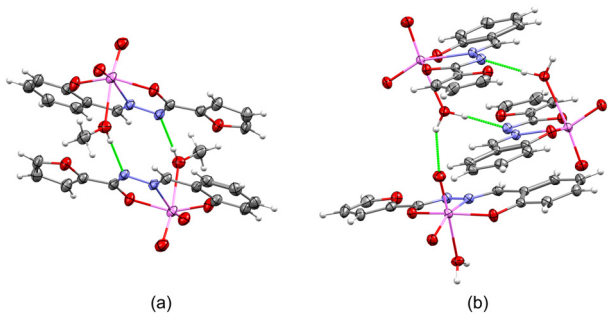

Fig. 1 Molecular and crystal structures of (a) $[MoO_2(L^1)(MeOH)]$ and (b) $[MoO_2(L^1)(H_2O)]$, showcasing the difference in hydrogen bonding (green lines).

Molecular modelling results

Density functional theory (DFT) calculations were performed to rationalize the experimentally observed coordination behavior and aggregation modes of the Mo(VI) complexes. In particular, the calculations were aimed at elucidating the role of solvent coordination. Previous studies indicate that Mo(VI) complexes formed in strong donor solvents usually exhibit solvent coordination at the sixth coordination site, while those formed in weakly coordinating solvents often contain oxygen atoms. In contrast, our experimental results show that reactions conducted in MeCN lead to the formation of water-coordinated species, an uncommon outcome in the reported literature. By comparing monomeric and dimeric models, the computational study provides a molecular-level explanation for the solvent-dependent speciation and the absence of μ-oxo dimers under experimental conditions.

Based on the determined crystal structures, two Mo(VI) mononuclear complexes were considered. One of them is methanol (**1**), while the other is water coordinated (**3**) (Fig. 2). To compare the energetic and structural properties of the compounds, DFT calculations were conducted. The distance between the azo nitrogen and molybdenum is slightly longer in the case of the methanol-coordinated complex compared to the water-coordinated scenario, but the difference is less than 0.01 Å. On the other hand, the distance between the oxygen of methanol and Mo compared to the water–Mo distance is

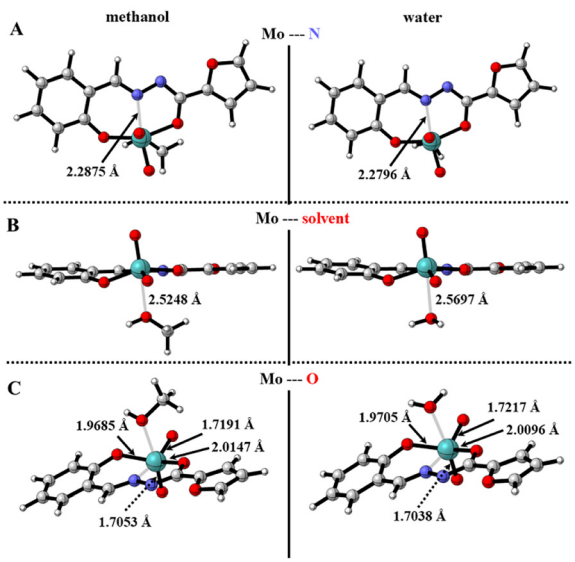

Fig. 2 Optimized structures of the studied methanol (left) and water (right) coordinated Mo(VI) complexes. For both complexes three different orientations are shown (A, B, and C). The corresponding structural information is also depicted in Å. Optimizations were conducted at the B3LYP/6-31G(d,p)/SDD level of theory.

shorter by slightly more than 0.04 Å in the optimized structures (Fig. 2B).

The other main interactions between the Mo centre and the two terminal oxygens and the oxygens of the ligand are also very similar in both cases. The largest difference is 0.0051 Å (Mo···O), while the smallest is 0.0015 Å (Mo═O) (Fig. 2C).

From these mononuclear structures, two specific types of oligomer – dimers – can be achieved. Dimers were chosen as the simplest type of oligomer. The first type is the solvent-assisted case, in which the dimer is formed *via* coordinated solvent molecules (methanol or water) (Fig. 3, left and middle) and other non-covalent interactions.

The second type is a μ-oxo dimer within which two metal centres (Mo atoms) are bridged *via* an oxygen directly forming a covalent Mo–O–Mo linkage (Fig. 3, right).

To model the structural features of the compounds and to understand the specific driving force behind why only solvent-assisted dimers were achieved experimentally, additional calculations were carried out. From a structural point of view, solvent-assisted dimers are again very similar and symmetrical (Fig. 3). The two Mo···N distances in both methanol and water-assisted dimers are basically identical. Furthermore, the difference between these structural features, when the two solvent-assisted cases are compared, is only 0.002 Å. The two molybdenum–nitrogen interactions in the μ-oxo dimer are also identical (2.3426 Å). However, when compared to the solvent-assisted scenarios, the Mo···N distance is about 0.04 Å longer in the μ-oxo dimer (Fig. 3). Similarly, the Mo···solvent and solvent···N interactions are very close to each other regardless of whether methanol or water coordination occurs. The difference is only 0.014 and 0.008 Å, respectively. Considering the μ-oxo dimer, it has its own specific symmetry as well. In the HO–Mo–O–Mo–OH backbone, the two HO–Mo and Mo–O bonds are almost identical to their counterparts in the chain, and the difference is only 0.0017 and 0.0078 Å, respectively.

Besides the obvious structural similarities and differences between the two specific types of dimers (solvent-assisted and μ-oxo types), their formation differs significantly. In the case of the solvent-assisted scenario, dimerization of the monomeric Mo(VI) complexes occurs *via* the formation of stabilizing hydrogen bonds due to the presence of solvents (methanol or water) (Fig. 4, middle and bottom). On the other hand, the formation of the μ-oxo dimer was envisaged as a condensation process between two monomeric units, involving deprotonation of a coordinated water molecule, protonation of a terminal oxo ligand, and subsequent elimination of water to yield a Mo–O–Mo bridge (Fig. 3, right, Fig. 4, top and SI Fig. S23). As a first step, deprotonation of a coordinated water molecule

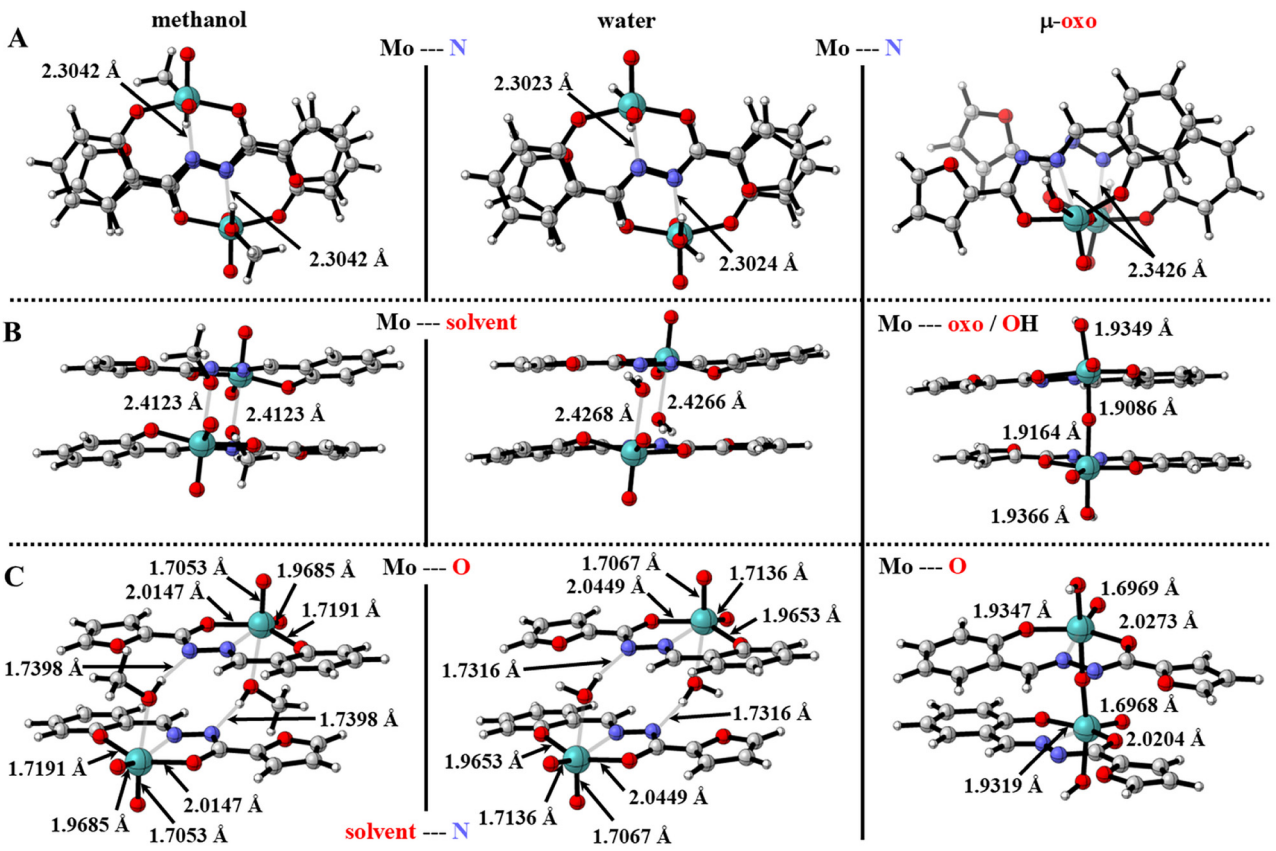

Fig. 3 Optimized structures of the studied Mo(VI) dimers: methanol (left), water (center), and μ-oxo (right). For each dimer three different orientations are shown (A, B, and C). The corresponding structural information is also depicted in Å. Optimizations were conducted at the B3LYP/6-31G(d, p)/SDD level of theory.

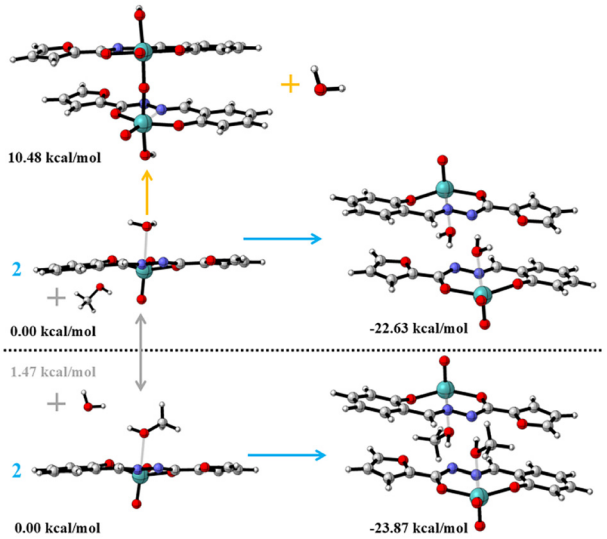

Fig. 4 Studied hypothetical reaction channels of the Mo(VI) compounds. Solvent coordinated dimerisations are indicated with blue, while the pathway leading to the formation of a dimer with an oxo bridge is indicated with orange. The water/methanol exchange was also studied and marked in grey. The corresponding reaction Gibbs free energies (DG_r) are also shown in kcal mol^{-1} calculated at the B3LYP/6-31G(d,p)/SDD level of theory.

from one of the corresponding monomers and protonation of terminal oxo ligands occur, leading to the formation of OH groups. Thus, the HO–Mo–O–Mo–OH backbone is achieved. The additional water molecule from the second monomer leaves the system as a side product (Fig. 4, top).

From a thermodynamic point of view, solvent-assisted dimerization is feasible in both water- and methanol-coordinated cases. In both cases, dimer formation is preferred by −22.63 and −23.87 kcal mol^{-1} for the water- and methanol-assisted systems, respectively. Considering the μ-oxo dimer, the reaction is endergonic, and the corresponding reaction Gibbs free energy is 10.48 kcal mol^{-1}. All in all, the significant preference for the solvent-assisted dimers might be the key reason why the μ-oxo dimer was not obtained during the preparation of the compounds.

Alternative μ-oxo motifs, such as symmetric Mo_2O_2 four-membered ring systems with two bridging oxo ligands, have been reported in the literature.[51] However, their formation would require a more extensive reorganization of the coordination sphere, which is not supported by the present experimental observations. In addition, the calculated positive Gibbs free energy indicates that μ-oxo dimer formation is thermodynamically disfavored under applied conditions.

Catalytic studies

The selective oxidation of benzyl alcohol to benzaldehyde, a key intermediate in pharmaceuticals,[4,5] food[6] and fragrance synthesis,[7] has driven the search for efficient, environmentally benign catalysts that work under mild conditions with green oxidants such as hydrogen peroxide and *tert*-butyl hydroperoxide in aqueous medium. In this study, a series of six molybdenum(VI) coordination complexes (**1–6**) were evaluated as catalysts for the oxidation of benzyl alcohol using TBHP in aqueous medium as the oxidant. The influence of oxidant loading on conversion and product selectivity was systematically investigated. Additionally, to gain further insight into the catalytic behaviour and co-solvent effects, two methanol-coordinated complexes (**1** and **2**) were tested using H_2O_2 as the oxidant in the presence of different amounts of acetonitrile as a co-solvent. Furthermore, the effect of reaction temperature (60 °C, 70 °C and 80 °C) on the performance of these two catalysts (**1** and **2**) was investigated to determine optimal conditions for maximising benzaldehyde selectivity. This study aims to identify operational parameters governing catalytic efficiency and selectivity in benzyl alcohol oxidation.

Oxidant role. The effect of oxidant loading on catalytic performance was systematically investigated by comparing two oxidant-to-substrate molar ratios (4 : 1 and 2 : 1) in the oxidation of benzyl alcohol. This approach was designed to evaluate how oxidant availability influences both conversion and product selectivity, providing insight into the interplay between oxidant concentration and catalyst efficiency. All experiments were conducted under identical conditions (80 °C, five hours) to ensure direct comparison. Key performance indicators are presented in Table 1 and Fig. 5 to highlight the influence of the oxidant amount on catalytic behaviour.

When comparing the catalytic performance of the investigated complexes (**1–6**) in terms of conversion, the mononuclear methanol-coordinated systems clearly outperform the other groups. $[MoO_2(L^1)(MeOH)]$ (**1**) exhibited the highest overall conversion of 43% at a lower 2 : 1 oxidant ratio, while $[MoO_2(L^2)(MeOH)]$ (**2**) reached 37%. In the literature it has been reported that nitro-substituted ligands generally enhance the catalytic activity of molybdenum complexes due to their electron-withdrawing character, which increases the electrophilicity of the metal centre and facilitates substrate activation.[52] Although the electron-withdrawing nitro group is expected to enhance oxidation by increasing the metal centre's redox potential, this effect does not appear to translate into improved catalytic performance at the lower oxidant-to-substrate ratio (2 : 1). Under tested conditions, $[MoO_2(L^1)(MeOH)]$ (**1**) shows higher conversion than $[MoO_2(L^2)(MeOH)]$ (**2**). This suggests that, in this system, electronic modulation by the nitro group offers limited benefit when oxidant availability is low, and that non-electronic factors such as steric influences or coordination stability may play a more significant role. When examining a higher oxidant-to-substrate ratio (4 : 1), a slight improvement is observed, with complex **2** showing a higher conversion rate than complex **1** (27% *vs.* 21%).

The water-coordinated analogues, $[MoO_2(L^1)(H_2O)]$ (**3**) and $[MoO_2(L^2)(H_2O)]$ (**4**), were less active, showing conversions below 12% at a 2 : 1 ratio and around 21–22% at a 4 : 1 ratio. The similarity in their performance suggests that ligand variation has minimal influence on catalytic activity under these conditions.

Table 1 Catalytic results of benzyl alcohol oxidation

	Catalyst	$[MoO_2(L^1)(MeOH)]$ (**1**)	$[MoO_2(L^2)(MeOH)]$ (**2**)	$[MoO_2(L^1)(H_2O)]$ (**3**)	$[MoO_2(L^2)(H_2O)]$ (**4**)	$[MoO_2(L^1)]_n$ (**5**)	$[MoO_2(L^2)]_n$ (**6**)
	Oxidant	TBHP in aqueous medium					
	Substrate	Benzyl alcohol					
4 : 1[e]	Con[a]/%	21	27	21	22	22	6
	Sel[b]/%	64	67	65	65	64	85
	$TOF_{20\ min}$ [c]	10	11	30	19	5	3
	TON[d]	42	52	42	42	44	12
2 : 1[f]	Con[a]/%	43	37	11	8	11	10
	Sel[b]/%	65	59	77	71	71	79
	$TOF_{20\ min}$ [c]	45	65	18	7	7	7
	TON[d]	88	78	22	15	22	19

Reaction conditions: time, 5 h; temperature, 80 °C. [a] Substrate consumed at the end of the reaction. [b] Formed aldehyde per converted alcohol at the end of the reaction. [c] *n*(substrate)transformed/*n*(catalyst)/time(h) at 20 min. [d] *n*(substrate)transformed/*n*(catalyst) at the end of the reaction. [e] *n*(catalyst)/*n*(benzyl alcohol)/*n*(oxidant) = 0.1 mmol/20 mmol/80 mmol. [f] *n*(catalyst)/*n*(benzyl alcohol)/*n*(oxidant) = 0.1 mmol/20 mmol/40 mmol. TBHP in aqueous medium was used as the oxidant.

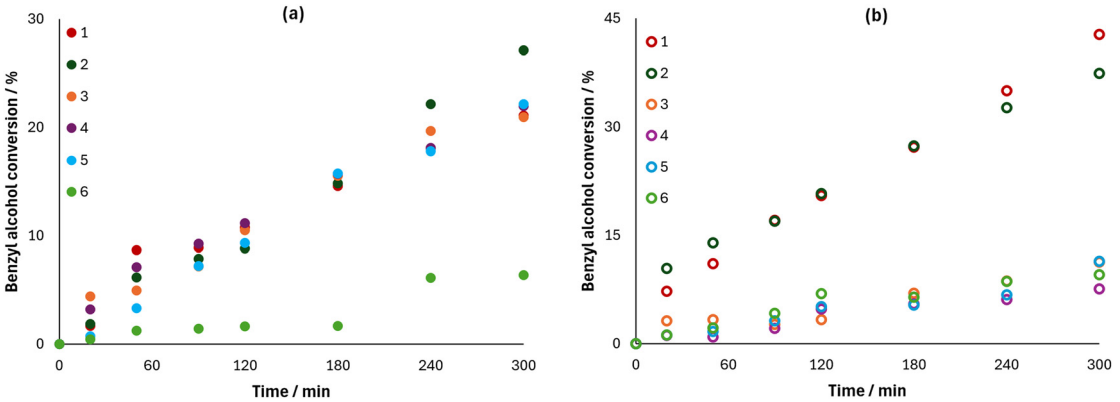

Fig. 5 Kinetic profiles of benzyl alcohol conversion for six molybdenum(VI) complexes (**1–6**). Reaction conditions: time, 5 h; temperature, 80 °C: (a) *n*(catalyst)/*n*(benzyl alcohol)/*n*(oxidant) = 0.1 mmol/20 mmol/80 mmol. (b) *n*(catalyst)/*n*(benzyl alcohol)/*n*(oxidant) = 0.1 mmol/20 mmol/40 mmol. TBHP in aqueous medium was used as the oxidant.

Lastly, the polynuclear systems $[MoO_2(L^1)]_n$ (**5**) and $[MoO_2(L^2)]_n$ (**6**) afforded similar conversions (6–22%) to the water-coordinated system. When the ratio was 2 : 1, the conversion results were comparable (10–11%); however, at a 4 : 1 ratio, complex **5** exhibited a significantly higher conversion (22%) compared to complex **6** (6%). This difference could be attributed to the possible steric hindrance imposed by the nitro group in the polymeric arrangement, which may limit substrate coordination under these conditions.

Selectivity trends, however, reveal a different picture. The methanol-coordinated complexes (**1** and **2**) produced moderate selectivity towards benzaldehyde (59–67%), consistent with their higher activity, which may accelerate over-oxidation pathways. In contrast, the water-coordinated complexes (**3** and **4**) exhibited higher selectivity (65–77%), suggesting that their lower reactivity imposes a more controlled oxidation process and restricts further oxidation. The polymeric complex $[MoO_2(L^1)]_n$ (**5**) showed similar selectivity to the water-coordinated complex (**3**). In contrast, the highest selectivity was observed for the polynuclear complex $[MoO_2(L^2)]_n$ (**6**), which consistently achieved 79–85% selectivity despite its moderate conversion. This could imply that its rigid polynuclear framework suppresses secondary transformations, favouring cleaner oxidation to benzaldehyde. Such a property could be particularly valuable in contexts where product purity is more critical than yield.

TON and $TOF_{20\ min}$ values reveal key differences in catalyst efficiency and initial activity. At a lower oxidant ratio (2 : 1), $[MoO_2(L^1)(MeOH)]$ (**1**) showed the highest TON (88) and a high $TOF_{20\ min}$ (45), indicating strong long-term performance and rapid initiation under mild conditions. Complex $[MoO_2(L^2)(MeOH)]$ (**2**) exhibited the highest $TOF_{20\ min}$ (65), at 2 : 1, reflecting very fast initiation, although its TON (78) was slightly lower, suggesting somewhat reduced sustained activity. Water-coordinated complexes (**3** and **4**) displayed lower TON and TOF values under both conditions, with little variation between ligands, suggesting limited influence of the ligand structure in these systems. Polynuclear complexes (**5** and **6**) showed the

lowest turnover, with TON values ranging between 12 and 44 and $TOF_{20\ min}$ values ranging between 3 and 7. This behaviour is consistent with reduced active site accessibility arising from steric constraints imposed by the polynuclear framework. Overall, methanol-coordinated complexes deliver the best catalytic efficiency, with complex **1** excelling in TON and complex **2** in $TOF_{20\ min}$, while water-coordinated and polynuclear catalysts show somewhat lower activity.

The conversion-selectivity plot (Fig. 6) offers a complementary perspective on catalytic behaviour, revealing how the complexes cluster at different oxidant ratios. At a 2 : 1 ratio, the methanol-coordinated complexes (**1** and **2**) form a distinct group in the high-conversion/medium-selectivity region, reflecting their ability to sustain higher activity even under reduced oxidant input, with selectivity in the range of 59 to 65%. In contrast, complexes **3**, **4**, **5**, and **6** group together at lower conversions but higher selectivity (71–79%), indicating a shift towards more controlled oxidation in systems where coordinated water or polynuclear frameworks impose steric and electronic constraints on the active site.

At a 4 : 1 oxidant ratio, complexes **1**, **3**, **4**, and **5** cluster closely in the moderate conversion (21–22%) and moderate selectivity (64–65%) range. This convergence of methanol-, water-, and polynuclear-based catalysts indicates that a higher concentration of TBHP in aqueous medium equalises the reactivity of otherwise distinct systems. This supports the idea that excess oxidant does not necessarily enhance catalytic turnover, but instead reduces the influence of the catalyst environment, leading to comparable performance across different catalyst classes.

Overall, these groupings show that under mild oxidant conditions, the metal centre coordination environment strongly dictates the performance: methanol promotes activity, while water and polynuclear environments favour selectivity. However, under higher oxidant conditions this effect is lost.

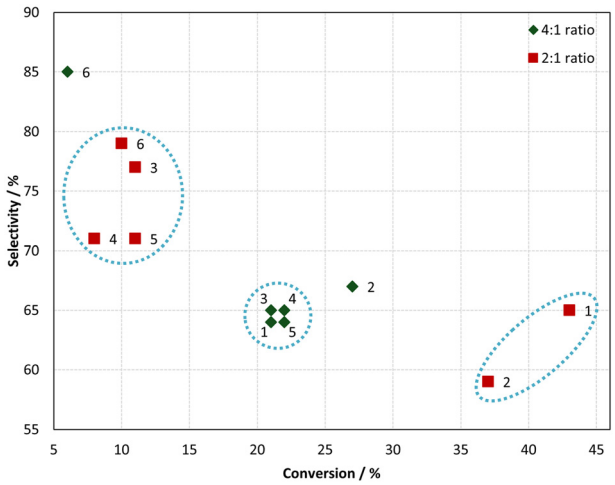

Fig. 6 Conversion *vs.* selectivity in benzyl alcohol oxidation using Mo (VI) catalysts (**1–6**) (TBHP in aqueous medium to benzyl alcohol at 4 : 1 (green) and 2 : 1 (red) ratios).

Acetonitrile role. The methanol-coordinated molybdenum (VI) complexes (**1** and **2**) were chosen for further study because initial screening with TBHP in aqueous medium identified them as the most promising candidates, showing the best balance of conversion and selectivity among the tested series. While TBHP in aqueous medium is often used as an oxidant in catalyst development due to its high reactivity, we shifted to hydrogen peroxide (H_2O_2) in further studies because it is a greener oxidant, producing only water as a by-product and is therefore more attractive for sustainable catalytic oxidation.[53] Although reactions with TBHP in aqueous medium performed at a lower oxidant-to-substrate ratio (2 : 1) gave better results than the H_2O_2 experiments, a 4 : 1 ratio was selected for further testing because preliminary trials at 2 : 1 showed very low conversion.

Moderate amounts of organic co-solvents (acetonitrile, acetone, chloroform, and methanol) are frequently employed in H_2O_2 oxidations to balance solubility with selective oxidant activation.[54,55] In this context, acetonitrile (MeCN) was introduced as a co-solvent, since literature reports consistently highlight its ability to improve substrate and catalyst solubility, stabilize metal-peroxo intermediates and moderate the reactivity of aqueous H_2O_2.[53,54,56] Guided by these results, three MeCN volumes (1.5, 3.0, and 6.0 mL) were examined to capture the effects of low, intermediate, and relatively high co-solvent loadings. The reaction temperature was set at 70 °C, slightly lower than the 80 °C used in the earlier testing with TBHP in aqueous medium, because hydrogen peroxide is more prone to thermal decomposition and milder conditions improve oxidant efficiency and selectivity. The catalytic results are summarized in Fig. 7 and 8.

At 1.5 mL MeCN, both complexes exhibited the highest substrate conversion (57% for **1** and 58% for **2**), indicative of rapid peroxide activation at low organic content. Selectivity toward benzaldehyde was comparatively low (2–3%), consistent with a highly reactive oxidizing environment.

At 3 mL MeCN, the conversion decreased (29% for **1** and 28% for **2**) as the increased organic fraction partially diluted the aqueous phase, thereby moderating peroxide availability. These conditions afforded a marked improvement in the selectivity (60% for **1** and 58% for **2**), suggesting that a moderate MeCN content facilitates a more controlled oxidation pathway, potentially through stabilization of metal-peroxo intermediates and improved solubilization of the substrate and product.

At 6 mL MeCN, the conversions were further reduced (13% for **1** and **2**), reflecting decreased peroxide activation. The selectivity was further enhanced (67% for **1** and 59% for **2**), consistent with slower peroxide activation and reduced radical character.

Analysis of TON and $TOF_{20\ min}$ reveals distinct trends across solvent conditions. Low MeCN loading (1.5 mL) delivered the highest $TOF_{20\ min}$ (262 for **1** and 242 for **2**) and TON values (118 for **1** and 123 for **2**). At 3 mL MeCN, $TOF_{20\ min}$ decreased (33 for **1** and 74 for **2**), while TON values were 57 for both complexes, indicating a balance between the reaction rate and

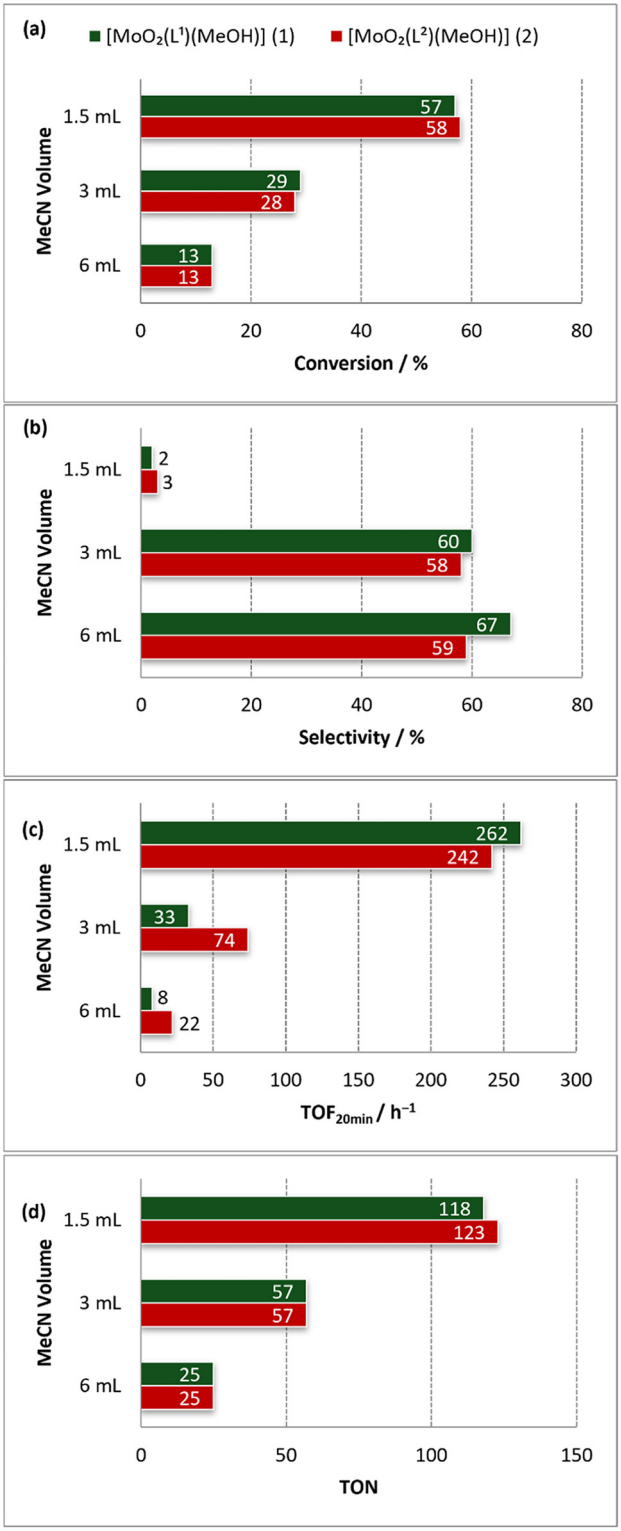

Fig. 7 Catalytic results of benzyl alcohol oxidation. Reaction conditions: time, 5 h; temperature, 70 °C, *n*(catalyst)/*n*(benzyl alcohol)/*n*(oxidant) = 0.1 mmol/20 mmol/80 mmol. H_2O_2 was used as the oxidant with the addition of acetonitrile. (a) Substrate consumed at the end of the reaction. (b) Aldehyde formed per converted alcohol at the end of the reaction. (c) *n*(substrate)transformed/*n*(catalyst)/time(h) at 20 min. (d) *n*(substrate)transformed/*n*(catalyst) at the end of the reaction.

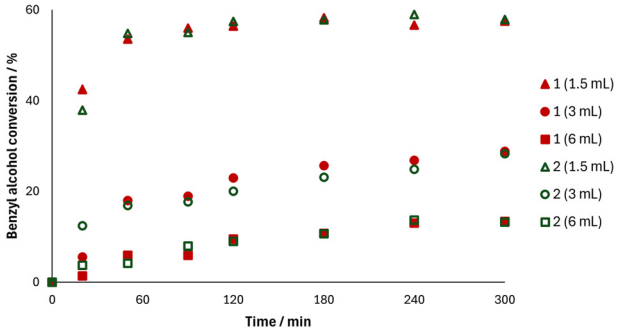

Fig. 8 Kinetic profiles of benzyl alcohol conversion for $[MoO_2(L^1)(MeOH)]$ (**1**) (red) and $[MoO_2(L^2)(MeOH)]$ (**2**) (green) when H_2O_2 was used as the oxidant with different amounts of acetonitrile added. Triangle – 1.5 mL, circle – 3 mL and square – 6 mL.

selectivity. At 6 mL MeCN, both $TOF_{20\ min}$ and TON were reduced ($TOF_{20\ min}$ = 8 for **1** and 22 for **2**; TON 25), while selectivity reached its maximum under these conditions. This variation in the initial catalytic activity with an increase in MeCN content likely reflects the beneficial role of co-solvent composition in modulating oxidant–catalyst interactions: a higher organic content can moderate the rate at which the oxidant reaches the active site, thereby offering finer control over the initiation of the oxidation process.

Complex **2** consistently exhibited a higher initial $TOF_{20\ min}$, particularly at an intermediate MeCN content, indicating a kinetic advantage in the early stages of the reaction. This faster initial rate reflects more rapid catalyst activation, which enhances early conversion but may influence the overall selectivity and catalyst stability. Such behaviour may be attributed to the effects of the nitro–substituted ligand discussed earlier. Overall, an intermediate MeCN (3 mL) content offers optimal catalytic performance.

Temperature role. Following the identification of 3 mL of MeCN as an optimal co-solvent volume for maintaining a balance between catalytic activity and selectivity in the oxidation of benzyl alcohol, a temperature screening study was conducted to further evaluate the influence of thermal input on the catalytic performance. Two complexes $[MoO_2(L^1)(MeOH)]$ (**1**) and $[MoO_2(L^2)(MeOH)]$ (**2**) were selected as representative systems, since previous results demonstrated that methanol-coordinated complexes exhibit greater catalytic performance compared to their water-coordinated analouges. Methanol-coordinated Mo(VI) complexes **1** and **2** were tested across different temperatures (60, 70 and 80 °C), while the polynuclear analogues $[MoO_2(L^1)]_n$ (**5**) and $[MoO_2(L^2)]_n$ (**6**) were examined only at 70 °C due to their limited catalytic efficiency. Reactions were carried out using H_2O_2 as an oxidant, maintaining a catalyst : benzyl alcohol : oxidant molar ratio of 0.1 : 20 : 80 mmol. All experiments were conducted over a period of five hours. The key catalytic metrics are presented in Table 2 and Fig. 9.

A clear temperature-dependent trend was observed for complexes **1** and **2**, with the catalytic activity generally increasing

Table 2 Catalytic results of benzyl alcohol oxidation

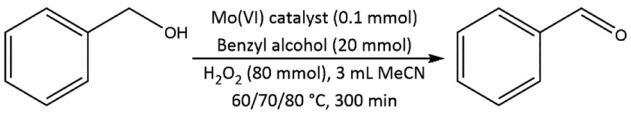

	Catalyst	$[MoO_2(L^1)(MeOH)]$ (**1**)	$[MoO_2(L^2)(MeOH)]$ (**2**)	$[MoO_2(L^1)]_n$ (**5**)	$[MoO_2(L^2)]_n$ (**6**)
80 °C	Con[a]/%	28	70	—	—
	Sel[b]/%	50	9	—	—
	$TOF_{20\ min}$ [c]	17	70	—	—
	TON[d]	57	139	—	—
70 °C	Con[a]/%	29	28	16	23
	Sel[b]/%	60	58	43	41
	$TOF_{20\ min}$ [c]	33	74	33	62
	TON[d]	57	57	31	46
60 °C	Con[a]/%	16	20	—	—
	Sel[b]/%	80	74	—	—
	$TOF_{20\ min}$ [c]	86	52	—	—
	TON[d]	31	39	—	—

[a] Substrate consumed at the end of the reaction. [b] Formed aldehyde per converted alcohol at the end of the reaction. [c] *n*(substrate)transformed/*n*(catalyst)/time(h) at 20 min. [d] *n*(substrate)transformed/*n*(catalyst) at the end of the reaction.

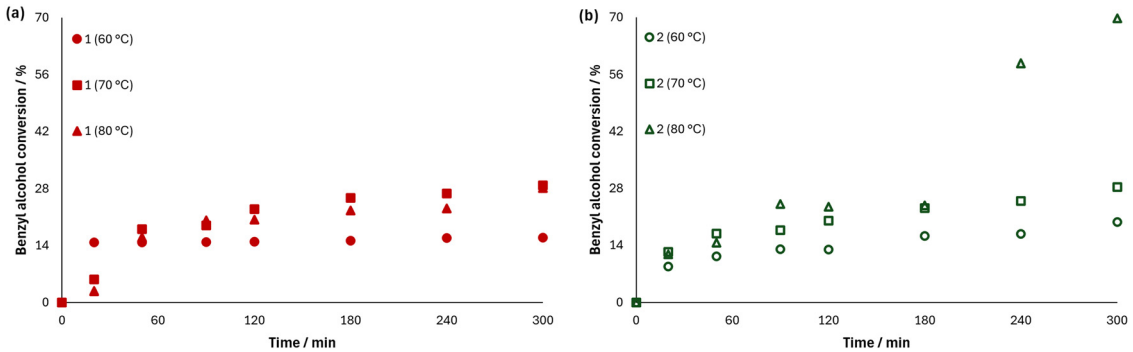

Fig. 9 Kinetic profiles of benzyl alcohol conversion for (a) $[MoO_2(L^1)(MeOH)]$ (**1**) (red) and (b) $[MoO_2(L^2)(MeOH)]$ (**2**) (green) with H_2O_2 and 3 mL of acetonitrile at different temperatures. Circle – 60 °C, square – 70 °C and triangle – 80 °C.

with temperature. At 80 °C, complex **2** exhibited the highest conversion within the series, reaching 70%, whereas complex **1** achieved 28% conversion. Selectivity toward benzaldehyde decreased under these conditions, with values of 9% for complex **2** and 50% for complex **1**. The observed decline in selectivity may be due to accelerated overoxidation processes, possibly leading to benzoic acid or further oxidative degradation, consistent with trends in some Mo(VI)-based catalytic systems.[57,58] This temperature effect reflects a trade-off between increased catalytic activity and diminished selectivity. Corresponding TON values were 139 for complex **2** and 57 for complex **1**, with $TOF_{20\ min}$ values of 70 and 33, respectively.

At 70 °C, the conversions were similar for both methanol-coordinated mononuclear complexes, with 29% for complex **1** and 28% for complex **2**. The selectivity was moderate, measuring 60% for complex **1** and 58% for complex **2**. TON values were 57 for complex **1** and 56 for complex **2**, while $TOF_{20\ min}$ values showed a notable difference, 33 for complex **1** and 74 for complex **2**, reflecting the faster initial turnover rate of complex **2**, likely due to the electron-withdrawing nature of ligand $\mathbf{H_2L^2}$ containing a nitro group. These values are consistent with earlier findings, where complex **2** demonstrated faster kinetic performance across varying co-solvent amounts and oxidant ratio systems. At 60 °C, both complexes displayed reduced conversions, with 16% for complex **1** and 20% for complex **2**.

Selectivity toward benzaldehyde was significantly improved under milder conditions, reaching 80% for complex **1** and 74% for complex **2**. TON values were 32 for complex **1** and 40 for complex **2**, with $TOF_{20\ min}$ values of 18 and 38, respectively. Again, complex **2** exhibited better results than complex **1**, possibly due to the nitro effect mentioned before. The obtained results are consistent with the literature, indicating that an increase in temperature leads to higher conversion but lower selectivity.[59,60–62]

The polynuclear complexes **5** and **6** were evaluated at 70 °C as a representative temperature. Their catalytic performances were modest, with conversion values of 16% (**5**) and 23% (**6**). However, selectivity values were lower than their mononuclear counterparts: 43% for complex **5** and 41% for complex **6**. Their corresponding TONs of 31 (**5**) and 46 (**6**) and $TOF_{20\ min}$ values (33 for complex **5** and 62 for complex **6**) indicate that complex **6** was more reactive during the early phase of the reaction. Given these comparatively lower efficiencies, temperature-dependent screening was not extended to complexes **5** and **6**, as the data at 70 °C suggested limited potential for improvement under more favourable thermal conditions.

A plausible mechanistic exploration, together with a comparison to other Mo(VI) systems, has been added to the SI under the headings "Plausible mechanistic explanation" and "Evaluation against comparable catalysts".

Experimental

Materials

The starting compounds included commercially available aldehydes and hydrazide (Fluka AG, BLDpharm, and ALDRICH), as well as the solvents MeCN, MeOH, DCM and acetone (Fluka), which were used without further purification. The starting complex $[MoO_2(acac)_2]$ (acac = $C_5H_7O_2$ = acetylacetonate) was prepared as described in the literature.[63,64]

Ligand synthesis

Solution-based synthesis:

The ligands were synthesized *via* the condensation of 2-furoic hydrazide (0.1923 g, 1.524 mmol) with either salicylaldehyde (0.160 mL, 0.1862 g, 1.524 mmol) to form $\mathbf{H_2L^1}$, or 2-hydroxy-5-nitrobenzaldehyde (0.2510 g, 1.524 mmol) to form $\mathbf{H_2L^2}$, in a 1 : 1 molar ratio using methanol (30 mL) as the solvent.

Brown crystals were obtained for the ligand $\mathbf{H_2L^1}$ and a yellow powder was obtained for the ligand $\mathbf{H_2L^2}$. The products were filtered and analysed by IR-ATR spectroscopy, DSC analysis and SCXRD.

Mechanochemical-based synthesis:

The ligands $\mathbf{H_2L^1}$ and $\mathbf{H_2L^2}$ were synthesized *via* a mechanochemical method.

For the preparation of $\mathbf{H_2L^1}$, 2-furoic hydrazide (0.0200 g, 0.1585 mmol) and salicylaldehyde (16.6 μL, 0.0387 g, 0.3171 mmol) were placed in a Teflon milling jar with a Teflon ball. Methanol (20 μL) was added, and the mixture was milled at 25 Hz for 30 minutes. The reaction afforded a light brown powder as the product.

For the synthesis of $\mathbf{H_2L^2}$, 2-furoic hydrazide (0.0200 g, 0.1585 mmol) and 2-hydroxy-5-nitrobenzaldehyde (0.0265 g, 0.1585 mmol) were placed in a Teflon jar with a Teflon ball, followed by the addition of methanol or ethanol (30 μL) as the grinding aid. The mixture was milled under the same conditions (25 Hz, 30 min), affording a light-yellow powder. The products were analysed by IR-ATR spectroscopy and compared to the products obtained from solution-based synthesis.

Mechanochemical synthesis provided yields of >99%.

$\mathbf{H_2L^1}$

Colour: brown; yield for solution-based synthesis: 61.4%. IR-ATR (cm^{-1}): 3228 (O–H), 3116 (C–H), 3056 (C–H), 1655 (C═O), 1609 (C═N). DSC: onset = 173 °C, E = 26.41 kJ mol^{-1}.

$\mathbf{H_2L^2}$

Colour: yellow; yield for solution-based synthesis: 77.0%. IR-ATR (cm^{-1}): 3275 (O–H), 3101 (C–H), 3062 (C–H), 1669 (C═O), 1611 (C═N). DSC: onset = 277 °C, E = 39.83 kJ mol^{-1}.

Molybdenum(VI) complexes

Mononuclear complexes

Methanol-coordinated complexes $[MoO_2(L^{1\ or\ 2})(MeOH)]$. Solution-based synthesis:

$\mathbf{H_2L^1}$ (0.0500 g, 0.2172 mmol) was dissolved in methanol (30 mL) in a 100 mL round-bottom flask. $[MoO_2(acac)_2]$ (0.0708 g, 0.2172 mmol) was then added to the solution in a 1 : 1 molar ratio. The reaction mixture was refluxed for three hours and then allowed to cool to room temperature. Orange crystals were obtained, filtered off, dried and analysed by IR-ATR spectroscopy, TGA/DSC analysis and SCXRD.

The same procedure was used to synthesize the complex with the ligand $\mathbf{H_2L^2}$. The ligand $\mathbf{H_2L^2}$ (0.0500 g, 0.1816 mmol) was dissolved in methanol (30 mL), followed by the addition of $[MoO_2(acac)_2]$ (0.0592 g, 0.1816 mmol) in a 1 : 1 molar ratio, resulting in the formation of a yellow powder. The solid product was filtered, dried and analysed by IR-ATR spectroscopy and TGA/DSC.

Mechanochemical-based synthesis:

The same mononuclear complex $[MoO_2(L^1)(MeOH)]$ (**1**) was obtained by mechanochemical synthesis. The ligand $\mathbf{H_2L^1}$ (0.0200 g, 0.0868 mmol) and $[MoO_2(acac)_2]$ (0.0283 g, 0.0868 mmol) were placed in a Teflon jar with a Teflon ball. 30 μL of methanol was added and milled for 60 min at 25 Hz. A yellow powder product was obtained. The product was analysed by IR-ATR spectroscopy and compared to the product obtained from solution-based synthesis (SI Fig. S15).

$[MoO_2(L^1)(MeOH)]$ (1)

Colour: orange; yield: 74.7%. IR-ATR (cm^{-1}): 3138 (C–H), 2938 (C–H) 1609 (C═N), 1516 (C═C), 1271 (C–O), 1046 (MeOH), 910 and 898 (Mo═O). TGA: $MeOH_{theo}$: 8.24%, $MeOH_{exp}$: 8.57%, MoO_{3theo}: 36.84%, MoO_{3exp}: 36.62%.

$[MoO_2(L^2)(MeOH)]$ (2)

Colour: yellow; yield: 67.8%. IR-ATR (cm^{-1}): 3142 (C–H), 1614 (C═N), 1509 (C═C), 1272 (C–O), 1054 (MeOH), 939 and 913 (Mo═O). TGA: $MeOH_{theo}$: 7.39%, $MeOH_{exp}$: 8.63%, MoO_{3theo}: 33.01%, MoO_{3exp}: 29.02%.

Water-coordinated complexes $[MoO_2(L^{1\ or\ 2})(H_2O)]$. Solution-based synthesis:

$\mathbf{H_2L^1}$ (0.0500 g, 0.2172 mmol) was dissolved in 30 mL of acetonitrile, acetone, or dichloromethane in a 100 mL round-bottom flask. To this solution, $[MoO_2(acac)_2]$ (0.0708 g, 0.2172 mmol) was added, maintaining a 1 : 1 molar ratio. The mixture was refluxed for three hours and then allowed to cool

to room temperature. The resulting orange crystals were filtered, dried and analysed by IR-ATR spectroscopy, TGA/DSC analysis and SCXRD.

The same procedure was used to synthesize the complex with the ligand $\mathbf{H_2L^2}$. The ligand $\mathbf{H_2L^2}$ (0.0500 g, 0.1816 mmol) was dissolved in acetonitrile, acetone, or dichloromethane (30 mL), followed by the addition of $[MoO_2(acac)_2]$ (0.0592 g, 0.1816 mmol) in a 1 : 1 molar ratio, resulting in the formation of a yellow powder. The solid product was filtered, dried and analysed by IR-ATR spectroscopy and TGA/DSC.

Mechanochemical-based synthesis:

The same mononuclear complex $[MoO_2(L^2)(H_2O)]$ (**4**) was obtained by mechanochemical synthesis. The ligand $\mathbf{H_2L^2}$ (0.0200 g, 0.0727 mmol) and $[MoO_2(acac)_2]$ (0.0283 g, 0.0868 mmol) were placed in a Teflon jar with a Teflon ball. 30 μL of methanol was added and milled for 120 min at 25 Hz. The jar was opened at 60 min for 10 min. A yellow powder product was obtained. The product was analysed by IR-ATR spectroscopy and compared to the product obtained from solution-based synthesis. The optimised reaction parameters are presented in SI Table S1.

$[MoO_2(L^1)(H_2O)]$ (3)

Colour: orange; yield: 20.4%. IR-ATR (cm^{-1}): 3127 (C–H), 1647 (H_2O), 1612 (C═N), 1554 (C═C), 1270 (C–O), 909 and 871 (Mo=O) TGA: H_2O_{theo}: 4.81%, H_2O_{exp}: 5.11%, MoO_{3theo}: 38.22%, MoO_{3exp}: 37.60%.

$[MoO_2(L^2)(H_2O)]$ (4)

Colour: yellow; yield: 40.0%. IR-ATR (cm^{-1}): 3463 (O–H), 3145 (C–H), 3084 (C–H), 1633 (H_2O), 1609 (C═N), 1503 (C═C), 1275 (C–O), 945 and 918 (Mo=O). TGA: H_2O_{theo}: 4.29%, H_2O_{exp}: 5.10%, MoO_{3theo}: 34.12%, MoO_{3exp}: 30.16%

Polynuclear complexes. If the mononuclear complex $[MoO_2(L^{1\text{ or }2})(MeOH)]$ or $[MoO_2(L^{1\text{ or }2})(H_2O)]$ is heated at 250 °C it turns into the brown polynuclear complex $[MoO_2(L^{1\text{ or }2})]_n$.

$[MoO_2(L^1)]_n$ (5)

Colour: brown; yield: 100%. IR-ATR (cm^{-1}): 3136 (C–H), 3039 (C–H), 1618 (C═N), 1526 (C═C), 1270 (C–O), 856 (Mo═O). TGA: MoO_{3theo}: 40.26%, MoO_{3exp}: 41.80%.

$[MoO_2(L^2)]_n$ (6)

Colour: brown; yield: 100%. IR-ATR (cm^{-1}): 3092 (C–H), 3000 (C–H), 1606 (C═N), 1515 (C═C), 1263 (C–O), 833 (Mo═O). TGA: MoO_{3theo}: 35.65%, MoO_{3exp}: 32.05%.

Methods

The prepared compounds were characterized by infrared attenuated total reflectance (IR-ATR) spectroscopy, thermogravimetric analysis (TGA), differential scanning calorimetry (DSC) and single crystal X-ray diffraction (SCXRD).

IR-ATR analysis was performed using a PerkinElmer Spectrum Two spectrometer equipped with a diamond ATR attachment. The measurement was carried out in the 4000–400 cm^{-1} range with four scans. The spectra were processed and analysed using Excel.

A Mettler–Toledo DSC823e instrument was used for differential scanning calorimetry (DSC) analysis in the range of 25–300 °C under an inert N_2 atmosphere with a flow rate of 50 mL min^{-1} and a heating rate of 10 °C min^{-1}. Measurements were conducted using closed aluminium containers featuring a single perforation in the lid. The obtained data were processed using Mettler STARe Evaluation Software v18.00.

Thermogravimetric (TGA) analysis was performed using a Mettler-Toledo TGA/DSC 3+ instrument in aluminium oxide crucibles equipped with lids containing a single perforation. All experiments were performed under an O_2 atmosphere with a flow rate of 200 cm^3 min^{-1} and a heating rate at 10 °C min^{-1}. The measurements were carried out over a wide temperature range of 25–600 °C. The results were processed using Mettler STARe Evaluation Software v18.00.

Crystallography

Single crystals of $[MoO_2(L^1)(MeOH)]$ (**1**) and $[MoO_2(L^1)(H_2O)]$ (**3**) of suitable quality were selected for X-ray diffraction studies. Data collection was performed using a Rigaku XtaLAB Synergy-S diffractometer equipped with a Dualflex source using Cu Kα radiation (λ = 1.54184 Å) and a HyPix detector. Diffraction data were acquired using ω-scan techniques at 170 K for compounds (**1**) and (**3**). The data were processed with the CrysAlisPro software package.[65] The initial structural solution was achieved using dual-space methods implemented in SHELXT,[66] followed by full-matrix least-squares refinement on F^2 using SHELXL.[67] Refinement included anisotropic displacement parameters for all non-hydrogen atoms. Hydrogen atoms bonded to carbon were positioned geometrically and refined using a riding model, with U_{iso} values set to $1.2U_{eq}$ for CH and CH_2 groups and $1.5U_{eq}$ for methyl groups. Hydrogen atoms bound to heteroatoms were located from difference Fourier maps during the final refinement stages. All SHELX operations were carried out within the Olex2 crystallographic interface.[68] Geometric calculations were performed using PLATON,[69] and molecular graphics were generated with Mercury.[70] A summary of crystallographic data is provided in Tables S2–S4 (SI). Crystallographic data have been deposited with the Cambridge Crystallographic Data Centre under deposition numbers CCDC 2528700 and 2528701.

Molecular modelling methods

The positions of heavy atoms and hydrogens were taken from experimentally determined crystal structures and used to create the corresponding input files for computational chemistry calculations. Additional structures were also designed by combining information from different sources. Density functional theory (DFT) calculations were carried out, and the initial structures were optimised using the B3LYP method.[71] The 6-31G(d) split valence basis set was used for the nonmetal atoms in the structures, while the Stuttgart–Dresden (SDD) effective core potential was applied for the metal atom (Mo).[72–74] Frequency calculations were carried out at the same B3LYP/6-31G(d,p)/SDD level of theory to confirm that all optimized structures were true minima. Grimme's dispersion correction was taken into account to improve the accuracy of the

results.[75] The Gaussian 16 program package was employed to carry out all calculations.[76]

Catalysis

The catalytic liquid-phase oxidation of benzyl alcohol was performed using molybdenum-based coordination complexes as catalysts in a magnetically stirred, three-necked 50 mL round-bottom flask equipped with a reflux air condenser. The reaction system comprised benzyl alcohol (20 mmol), an oxidant either TBHP in aqueous medium (40 or 80 mmol) or H_2O_2 (80 mmol) in the presence of variable amounts of acetonitrile (for H_2O_2-based systems), biphenyl (0.75 mmol) as an internal standard, and a catalyst (0.1 mmol). The reactions were conducted at 80 °C for TBHP systems and at 60, 70, or 80 °C for H_2O_2/acetonitrile systems, under continuous stirring for five hours. At defined time intervals, aliquots were withdrawn, immediately diluted with diethyl ether, and subjected to gas chromatography (GC) analysis.

GC analyses were carried out using an Agilent 8860 gas chromatograph (Agilent Technologies, Santa Clara, CA, USA) equipped with a flame ionization detector (FID) and an HP-5 capillary column (30 m × 0.32 mm × 0.25 μm), with helium as the carrier gas. The injection port and detector temperatures were maintained at 250 °C and 200 °C, respectively. Quantification was achieved using calibration curves generated from authentic standards of all relevant species. Benzyl alcohol conversion and aldehyde formation were calculated relative to the biphenyl internal standard, with calibration curves exhibiting excellent linearity (r^2 = 0.999).

All reactions were conducted under homogeneous conditions, with the catalyst being fully dissolved as a molecular species in the reaction medium; thus, conventional heterogeneous catalyst recycling protocols were not applicable.

Conclusions

Six new Mo(VI) complexes, including mononuclear and polynuclear species, were synthesized using mechanochemical and solution-based approaches and fully characterized. Emphasis was placed on evaluating mechanochemical synthetic pathways and catalytic oxidation using environmentally benign oxidants, especially H_2O_2 in aqueous media, in line with green chemistry principles. Catalytic studies revealed a strong dependence on the coordination environment and nuclearity: methanol-coordinated mononuclear complexes exhibited the highest activity and turnover numbers, whereas water-coordinated and polynuclear systems showed lower activity but enhanced selectivity toward benzaldehyde. The influence of oxidant ratio, co-solvent volume, temperature, and ligand electronics enabled rational tuning of conversion–selectivity relationships, providing guidance for the design of efficient and sustainable Mo(VI)-based oxidation catalysts. DFT calculations showed that solvent donor ability dictates the coordination environment of the Mo(VI) centre. In methanol, the solvent readily coordinates, yielding a methanol-bound complex, whereas in weakly coordinating acetonitrile, trace water preferentially occupies the coordination site. In both cases, dimerization proceeds *via* strongly favoured solvent-assisted hydrogen-bonding interactions, while μ-oxo dimer formation through terminal oxo ligands is thermodynamically disfavoured. This pronounced energetic preference rationalizes the experimentally observed coordination behaviour and the absence of μ-oxo dimers under applied conditions.

Author contributions

Conceptualization: J. P. Data curation: J. S. and B. F. Formal analysis: J. S. and B. F. Funding acquisition: J. P. Investigation: J. P, J. S., and B. F. Methodology: J. S. and B. F. Project administration: J. P. Resources: J. P. Software: J. S. and B. F. Supervision: J. P. Validation: J. S. and B. F. Visualization: J. P., J. S., and B. F. Writing – original draft: J. P., J. S., and B. F. Writing – review & editing: J. P., J. S., and B. F.

Conflicts of interest

There are no conflicts to declare.

Data availability

The data supporting this article have been included as part of the supplementary information (SI). Supplementary information: IR-ATR spectra of ligand and complexes, DSC curves of the ligands, TGA of the complexes, crystallographic data for $[MoO_2(L^1)(MeOH)]$ and $[MoO_2(L^1)(H_2O)]$, optimised data for the structures, Plausible mechanism explanation, UV-Vis data and Evaluation against comparable catalysts. See DOI: https://doi.org/10.1039/d6dt00558f.

CCDC 2528700 and 2528701 contain the supplementary crystallographic data for this paper.[77a,b]

Acknowledgements

J. S. and J. P. acknowledge the support from the project CIuK (grant KK.01.1.1.02.0016) co-financed by the Croatian Government and the European Union through the European Regional Development Fund-Competitiveness and Cohesion Operational Programme. The GITDA (Governmental Information-Technology Development Agency, Hungary) is gratefully acknowledged for allocating computing resources used in this work. Calculations have also been carried out using resources provided by the Wroclaw Centre for Networking and Supercomputing (https://wcss.pl).

References

1 M. Pagliaro, S. Campestrini and R. Ciriminna, *Chem. Soc. Rev.*, 2005, **34**, 837–845.

2 M. Vazylyev, D. Sloboda-Rozner, A. Haimov, G. Maayan and R. Neumann, *Top. Catal.*, 2005, **34**, 93–99.
3 A. Jia, L.-L. Lou, C. Zhang, Y. Zhang and S. Liu, *J. Mol. Catal. A: Chem.*, 2009, **306**, 123–129.
4 S. Caron, R. W. Dugger, S. G. Ruggeri, J. A. Ragan and D. H. B. Ripin, *Chem. Rev.*, 2006, **106**, 2943–2989.
5 R. J. J. Jachuck, D. K. Selvaraj and R. S. Varma, *Green Chem.*, 2006, **8**, 29–33.
6 L. Marilleyand and M. G. Casey, *Int. J. Food Microbiol.*, 2004, **90**, 139–159.
7 A. Andersen, Int. J. Toxicol., 2006, **25**, 11–27.
8 C. D. Pina, E. Falletta and M. Rossi, *J. Catal.*, 2008, **260**, 384–386.
9 F. Adam and W. T. Ooi, *Appl. Catal., A*, 2012, **445–446**, 252–260.
10 Grand View Research, Benzaldehyde market size, share & trends analysis report by application (flavor & fragrance, pharmaceutical, agrochemical, cosmetics), by region, and segment forecasts, 2025–2030, GVR-4-68040-523-0, Grand View Research, San Francisco, 2024.
11 S. W. Kshirsagar, N. R. Patil and S. D. Samant, *Tetrahedron Lett.*, 2008, **49**, 1160–1626.
12 X. Wang, X. Shi, S. Gao, G. Xu, J. Yang, J. Guo and L. Dai, *New J. Chem.*, 2024, **48**, 11259–11266.
13 A. Kumar, V. P. Kumar, A. Srikanth, V. Vishwanathan and K. V. R. Chary, *Catal. Lett.*, 2016, **146**, 35–46.
14 C. Della Pina, E. Falletta and M. Rossi, *J. Catal.*, 2008, **260**, 384–386.
15 N. Idaka, S. Nishiyama and S. Tsuruya, *Phys. Chem. Chem. Phys.*, 2001, **3**, 1918–1924.
16 L. Liu, X. Zhou, C. Xin, B. Zhang, G. Zhang, S. Li, L. Liu and X. Tai, *RSC Adv.*, 2023, **13**, 23648.
17 J. K. Mobley and M. Crocker, *RSC Adv.*, 2015, **5**, 65780.
18 M. J. Ndolomingo and R. Meijboom, *Appl. Surf. Sci.*, 2017, **398**, 19–32.
19 J. K. Mobley and M. Crocker, *RSC Adv.*, 2015, **5**, 65780–65797.
20 E. Topić, J. Sarjanović, D. Musija, M. Mandarić, T. Hrenar, J. Pisk and V. Vrdoljak, *RSC Adv.*, 2025, **15**, 3547.
21 E. Topić, J. Sarjanović, D. Musija, M. Mandarić, A. Cocut, T. Hrenar, D. Agustin, J. Pisk and V. Vrdoljak, *Dalton Trans.*, 2025, **54**, 5532.
22 D. Kuzman, M. Pajić, L. Drempetić, J. Sarjanović, J. Pisk, M. Cindrić and V. Vrdoljak, *ACS Omega*, 2025, **10**, 16668–166682.
23 C. M. Crombie, R. J. Lewis, R. L. Taylor, D. J. Morgan, T. E. Davies, A. Folli, D. M. Murphy, J. K. Edwards, J. Qi, H. Jiang, C. J. Kiely, X. Liu, M. S. Skjøth-Rasmussen and G. J. Hutchings, *ACS Catal.*, 2021, **11**, 2701–2714.
24 A. Hommes, B. Dissselhorst and J. Yue, *AIChE J.*, 2020, **66**, e17005.
25 E. Nowcicka, J. P. Hofmann, S. F. Parker, M. Sankar, G. M. Lari, S. A. Kondrat, D. W. Knight, D. Bethell, B. M. Weckhuysen and G. J. Hutchiings, *Phys. Chem. Chem. Phys.*, 2013, **15**, 12147.
26 B. Monteiro, S. Gago, P. Neves, A. A. Valente, I. S. Gonçalves, C. C. L. Pereira, C. M. Silva and M. Pillinger, *Catal. Lett.*, 2009, **129**, 350–357.
27 A. V. Biradar, M. K. Dongare and S. B. Umbarkar, *Tetrahedron Lett.*, 2009, **50**, 2885–2888.
28 M. S. S. Adam, *Appl. Organomet. Chem.*, 2018, **32**, e4234.
29 L.-Z. Geng, J. Xing, W. Wei and Y.-Z. Zhou, *Jiegou Huaxue*, 2012, **31**, 562.
30 S. Gurunath, B. Atanu, S. Rajib, M. Monalisa, L. Sudhir, R. T. T. Edward and D. Rupam, *Inorg. Chem.*, 2021, **60**, 15291.
31 M. R. Maurya, S. Agarwal, C. Bader, M. Ebel and D. Rehder, *Dalton Trans.*, 2005, 537–544.
32 V. Arumugam, W. Kaminsky, N. S. P. Bhuvanesh and D. Nallasamy, *RSC Adv.*, 2015, **5**, 59428.
33 F. Borbone, A. Carella, U. Caruso, G. Roviello, A. Tuzi, P. Dardano, S. Lettieri, P. Maddalena and A. Barsella, *Eur. J. Inorg. Chem.*, 2008, **2008**, 1846.
34 S. Kumar and M. Nath, *J. Organomet. Chem.*, 2018, **856**, 87.
35 T. Sedaghat, L. Tahmasbi, H. Motamedi, R. Reyes-Martinez and D. Morales-Morales, *J. Coord. Chem.*, 2013, **66**, 712.
36 P. M. Haba, O. Diouf, A. Sy, M. L. Gaye, A. S. Sall, A. H. Barry and T. Jouini, *Z. Kristallogr. – New Cryst. Struct.*, 2005, **220**, 479.
37 J. P. Rada, B. S. M. Bastos, L. Anselmino, C. H. J. Franco, M. Lanznaster, R. Diniz, C. O. Fernández, M. Menacho-Márquez, A. M. Percebom and N. A. Rey, *Inorg. Chem.*, 2019, **58**, 8800.
38 N. K. Ngan, K. M. Lo, C. Seng and R. Wong, *Polyhedron*, 2011, **30**, 2922.
39 N. K. Ngan, R. C. S. Wong, K. M. Lo and S. W. Ng, *Acta Crystallogr., Sect. E:Struct. Rep. Online*, 2011, **67**, m748.
40 J. Shi, Y. Wei, Y. Zhang, J. Tang, H. Bian, Q. Yu and F. Huang, *Polyhedron*, 2019, **162**, 81–90.
41 Z. H. Chohan, M. A. Farooq, A. Scozzafava and C. T. Supuran, *J. Enzyme Inhib. Med. Chem.*, 2002, **17**, 1–7.
42 M. R. Maurya, N. Jangra, F. Avecilla and I. Correia, *Eur. J. Inorg. Chem.*, 2019, **2019**, 314.
43 J. Sarjanović, M. Stojić, M. Rubčić, L. Pavić and J. Pisk, *Materials*, 2023, **16**, 1064.
44 J. Sarjanović, M. Cader, E. Topić, M. Razum, D. Agustin, M. Rubčić, L. Pavić and J. Pisk, *Mater. Adv.*, 2024, **5**, 9391–9402.
45 J. Pisk, M. Šušković, E. Topić, D. Agustin, N. Judaš and L. Pavić, *Int. J. Mol. Sci.*, 2024, **25**, 4859.
46 J. P. Thielemann, J. Kröhnert and C. Hess, *J. Phys. Chem.*, 2010, **114**, 17092–17098.
47 S. Mrkonja, M. Pajski, E. Topić, D. Agustin and J. Pisk, *Eur. J. Inorg. Chem.*, 2024, **27**, e202400350.
48 J. Sarjanović, M. Razum, B. Fiser, L. Pavić and J. Pisk, *J. Mater. Chem. C*, 2026, **14**, 2439–2453.
49 R. Bikas, H. H. Monfared, C. Kazak, N. B. Arslan and K. Bijanzad, *Acta Crystallogr., Sect. E:Struct. Rep. Online*, 2010, **66**, o2015.
50 M. Sennappan, P. M. Krishna and R. Hari Krishna, *J. Mol. Struct.*, 2019, **1178**, 333.
51 Z. Anorg, *Allg. Chem.*, 2009, **635**, 2120–2125.

52 W. Wang, T. Guerrero, S. R. Merecias, H. García-Ortega, R. Santillan, J.-C. Daran, N. Farfán, D. Agustin and R. Poli, *Inorg. Chim. Acta*, 2015, **431**, 176–183.
53 R. Goyal, O. Singh, A. Agrawal, C. Samanta and B. Sarkar, *Catal. Rev.*, 2022, **64**, 229–285.
54 M. Alizadeh and B. Yadollahi, *RSC Adv.*, 2025, **15**, 8777.
55 A. Corma, P. Esteve and A. Martínez, *J. Catal.*, 1996, **161**, 11–19.
56 X. Liu, S. Yang, L. Yang, H. Yu, T. Zhang and W. Wang, *J. Chem. Eng. Theor. Appl. Chem.*, 2023, **80**, 35–50.
57 C. Bersani, D. Rodríguez-Padrón, D. Ballesteros, E. Rodríguez-Castellón, A. Perosa and M. Selva, *ChemSusChem*, 2025, **18**, e202400888.
58 X.-Y. Si and J.-F. Wei, *J. Mol. Catal. A: Chem.*, 2005, **229**, 13–17.
59 N. Heydari, R. Bikas, M. Shaterian and T. Lis, *Appl. Organomet. Chem.*, 2023, **37**, e6939.
60 J. M. Deshmukh, L. H. Mahind, S. A. Waghmode and S. P. Dagade, *Asian J. Chem.*, 2017, **29**, 1455–1458.
61 A. V. Biradar, M. K. Dongare and S. B. Umbarkar, *Tetrahedron Lett.*, 2009, **50**, 2885–2888.
62 H. Liu, Z. Zhuo, Y. Zhang, H. Wei, W. Zhang, T. Li, Z. Mao and W. Wang, *Int. J. Chem. Kinet.*, 2021, **53**, 1253–1261.
63 G. J.-J. Chen, J. W. McDonald and W. E. Newton, *Inorg. Chem.*, 1976, **15**, 2612–2615.
64 S.-B. Yu and R. H. Holm, *Inorg. Chem.*, 1989, **28**, 4385–4391.
65 *Rigaku Oxford Diffraction. CrysAlisPro Software System, Versions 1.171.42.49, 1.171.41.92a, 1.171.41.93a and 1.171.42.53a, Rigaku Oxford Diffraction*, Oxford, UK, 2020.
66 G. M. Sheldrick, *Acta Crystallogr., Sect. A: Found. Adv.*, 2015, **71**, 3–8.
67 G. M. Sheldrick, *Acta Crystallogr., Sect. C: Struct. Chem.*, 2015, **71**, 3–8.
68 O. V. Dolomanov, L. J. Bourhis, R. J. Gildea, J. A. K. Howard and H. Puschmann, *J. Appl. Crystallogr.*, 2009, **42**, 339–341.
69 A. L. Spek, *Acta Crystallogr., Sect. D: Biol. Crystallogr.*, 2009, **65**, 148–155.
70 C. F. Macrae, I. Sovago, S. J. Cottrell, P. T. A. Galek, P. McCabe, E. Pidcock, M. Platings, G. P. Shields, J. S. Stevens, M. Towler and P. A. Wood, *J. Appl. Crystallogr.*, 2020, **53**, 226–235.
71 A. D. Becke, *J. Chem. Phys.*, 1993, **98**, 5648–5652.
72 T. H. Dunning Jr and P. J. Hay, in *Modern Theoretical Chemistry*, ed. H. F. Schaefer III, Plenum, New York, 1977, vol. 3, pp. 1–28.
73 P. Fuentealba, H. Preuss, H. Stoll and L. Von Szentpály, *Chem. Phys. Lett.*, 1982, **89**, 418–422.
74 D. Andrae, U. Haeussermann, M. Dolg, H. Stoll and H. Preuss, *Theor. Chem. Acc.*, 1990, **77**, 123–141.
75 S. Grimme, J. Antony, S. Ehrlich and H. Krieg, *J. Chem. Phys.*, 2010, **132**, 154104.
76 M. J. Frisch, G. W. Trucks, H. B. Schlegel, G. E. Scuseria, M. A. Robb, J. R. Cheeseman, G. Scalmani, V. Barone, B. Mennucci, G. A. Petersson, H. Nakatsuji, M. Caricato, X. Li, H. P. Hratchian, A. F. Izmaylov, J. Bloino, G. Zheng, J. L. Sonnenberg, M. Hada, M. Ehara, K. Toyota, R. Fukuda, J. Hasegawa, M. Ishida, T. Nakajima, Y. Honda, O. Kitao, H. Nakai, T. Vreven, J. A. Montgomery Jr., J. E. Peralta, F. Ogliaro, M. Bearpark, J. J. Heyd, E. Brothers, K. N. Staroverov, R. Kobayashi, J. Normand, K. Raghavachari, A. Rendell, J. C. Burant, S. S. Iyengar, J. Tomasi, M. Cossi, N. Rega, N. J. Millam, M. Klene, J. E. Knox, J. B. Cross, V. Bakken, C. Adamo, J. Jaramillo, R. Gomperts, R. E. Stratmann, O. Yazyev, A. J. Austin, R. Cammi, C. Pomelli, W. J. Ochterski, R. L. Martin, K. Morokuma, V. G. Zakrzewski, G. A. Voth, P. Salvador, J. J. Dannenberg, S. Dapprich, A. D. Daniels, Ö. Farkas, J. B. Foresman, J. V. Ortiz, J. Cioslowski and D. J. Fox, *Gaussian 19, Revision C.01*, Gaussian, Inc, Wallingford CT, 2016.
77 (*a*) CCDC 2528700: Experimental Crystal Structure Determination, 2026, DOI: 10.5517/ccdc.csd.cc2qw9zx; (*b*) CCDC 2528701: Experimental Crystal Structure Determination, 2026, DOI: 10.5517/ccdc.csd.cc2qwb0z.